Observation of alternately localized Faraday waves in a narrow tank

Zhigang Zhu,[1] Yalei Song,[1] Xiaonan Liu,[1] Dawu Xiao,[1,*] Lei Yang,[2] and Liang Huang[1,†]

[1]*School of Physical Science and Technology and Institute of Computational Physics and Complex Systems, Lanzhou University, Lanzhou, Gansu 730000, China*

[2]*Institute of Modern Physics of CAS, Lanzhou, Gansu 730000, China*

(Received 27 June 2018; published 22 January 2019)

There are many experimental works and analyses of gravity water surface waves in vibrating high-aspect-ratio rectangular tanks. In most cases, the waves are symmetric or antisymmetric in the direction along the short sides. Here we report an unusual alternately localized Faraday wave (ALFW) in this system which is neither symmetric nor antisymmetric along the short side direction. The peculiar feature is that close to the boundary there are a series of large oscillating regions and flat regions; i.e., the surface barely moves during the experiment. The large oscillating regions and the flat regions appear alternately not only in the direction along the long side of the tank, but also along the short side. The large surface deformation implies strong nonlinearities of the phenomenon. The spectrum of the discrete cosine transformation of the surface profile shows clearly that there are only two dominating modes. However, further analyses reveal that it is not simply a two-mode excitation through external driving, but a one mode excitation, then pumping the other mode excited through strong internal mode interactions in a leading-passive way. We use the phenomenological nonlinear mode competition model, which is a set of coupled nonlinear Mathieu equations, to reproduce the ALFW pattern. Theoretical analyses and numerical simulations indicate that both nonlinear internal mode interactions and nonlinear bounding effects account for this phenomenon. Phase locking and amplitude bounding can be reproduced quantitatively by the model. The instability boundary in the parameter space obtained by numerical simulations fits the one obtained by experiments very well.

DOI: 10.1103/PhysRevFluids.4.014807

I. INTRODUCTION

Since the first report of Faraday waves in experiments [1], a numerous experimental [2–9], theoretical [10–18], and numerical [19–28] works among others have been devoted to the study of parametrically driven gravity surface waves. In addition, extensive investigations have been devoted to exploiting new surface wave patterns in the past few decades [29–39]. A variety of ordered wave patterns, such as triangles [30], quasipatterns that have no discrete translational symmetry [32], superlattice patterns [4,33,37,40], localized waves [35,37,38], and patterns stemming from various types of dispersions that depend on the depth of the fluid [41,42], intricate nonlinear surface dynamics [13,43], different boundary shapes of the containers [32,44–46], and directions of driving forces [5,47], have been observed in Faraday waves. Indeed, there exist comprehensive review articles and books on this subject [48,49]. Now there are good understandings of the physical mechanism underlying Faraday waves in an ideal fluid [48–52], where the onset of instability of the normal modes resulting from parametric resonance is governed by the Mathieu equation [52]. Note that this type of stability analysis is completely linear. It is known that the parametric instability

*Present address: Beijing Computational Science Research Center, Beijing 100084, China.
†huangl@lzu.edu.cn

in the Mathieu equation leads to exponential divergence of the solution [10,53]. The introduction of linear damping can only modify the instability boundary, but is not enough to bring the unstable solution bounded. It is actually the inherent nonlinearity of the surface wave that limits the growth of the amplitude [48,54]. Thus the nonlinear effects always play an important role in shaping the experimentally observed patterns of Faraday waves [8,48,49].

In recent years, with the development of experimental techniques and instruments, new types of Faraday wave patterns have been observed in experiments, such as star-shaped gravity surface waves in a cylindrical container [34] and highly localized oscillations aligned along one direction of rectangular tanks [39]. In particular, with high viscosity, Edwards *et al.* [32] found various patterns that are independent of the shapes of the containers. In this paper, we report the observation of a 3D Faraday wave pattern, having as many as five separated regions with large oscillations that unilaterally localized in a narrow (the aspect ratio is $L/b = 9.091$) rectangular tank, which is driven harmonically in the vertical direction. In particular, the localized wave has structure in both directions of the tank; that is, when the localized wave has large amplitudes on one side along the long boundary, it will be almost flat on the opposite side all the time, and the flat and large oscillation regions appear alternately along the long boundary.

In finite extended systems, the dissipation cannot be neglected [55,56]. Pattern formations are well described in terms of a few spatial modes; in particular, Douady and Fauve investigated pattern selection rules in the Faraday instability [4], and Residori *et al.* investigated two-mode competition phenomena [7], and the time evolution of the pattern is then related to the evolution of the coefficients of these modes [36]. Equations of coefficients have been developed for describing forced nonlinear surface wave systems [54,57,58], and the dissipation rates can be obtained by fitting the instability curves under linear conditions and added to the mode equations phenomenologically. In this article, the inviscid Euler-Lagrange formula, derived by Miles [13], is linearized to perform the stability analysis. Due to the significant high amplitudes of the pattern, nonlinearities will be taken into consideration and the mode competition equations used in [54] are adopted to model our system, which give good descriptions to the experiments.

The rest of the paper is organized as follows. In Sec. II, the parameters of the experimental setup are given. We present the main features of the localized water surface wave observed in our experiment, followed by a description of the evolution of the surface profile, both in real space and in mode space, which characterizes clearly how the alternately localized Faraday wave (ALFW) pattern is developed. The wave profiles for different driving frequencies are also provided, and the frequency range where the ALFW pattern can emerge is determined.

We give basic formulas governing water surface waves and boundary conditions in Sec. III. Through linear approximation, the parametric resonance between the response mode and the external driven force is revealed in Sec. IV.

Because of the moderately strong driven force and the existence of both parametric and internal resonances, nonlinearities will play an important role in shaping the localized pattern in our experiment. We adopt a phenomenological nonlinear model [54] to formulate the observed pattern and provide a physical illustration of its validity in Sec. V. In Sec. VI, we derive the coefficients of the nonlinear model by fitting to the experimental data and give an estimation of the uncertainties of these coefficients. Besides, a representative solution of the nonlinear model for the time evolution of the two modes is compared with the data obtained from experiments. Both amplitude bounding and phase-locking phenomena are revealed in the simulations, and they coincide with the experimental data very well.

Our discussion and the conclusion of our work are provided in Sec. VII.

II. EXPERIMENTS

A. Experimental setup

In our experiment, a plexiglas rectangular tank (Fig. 1) with aspect ratio 9.091 is partially filled with high-purity water. The length L and width b of the tank are 50.0 cm and 5.5 cm, respectively.

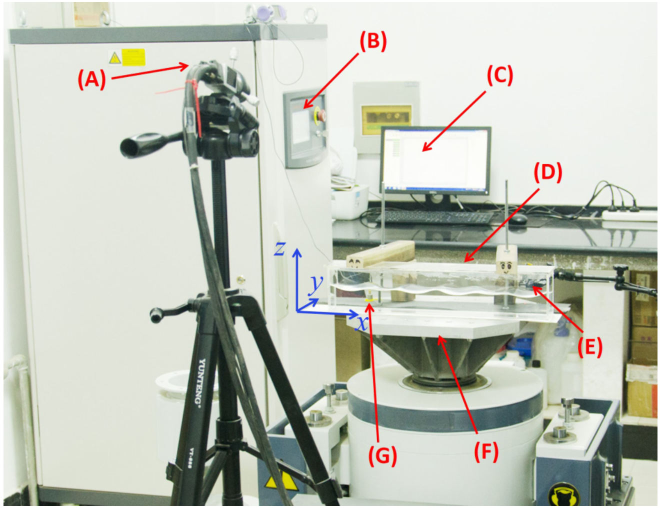

FIG. 1. The experimental setup. (A) The high-speed CMOS camera (Basler, acA2040-180 km, 180 fps at 2048×2048) that records the front side profile of the water surface wave. (B) The closed-loop power amplifier that generates the harmonic signal and drives the vibrator. (C) The computer with the software to set parameters of the power amplifier. (D) The tank that is partially filled with water. The length in the x direction is $L = 50.0$ cm, the width in the y direction is $b = 5.5$ cm, and the depth of the water at rest is $d = 5.0$ cm. (E) The laser range finder. (F) The vibrator. (G) The accelerometer that is attached to the vibration platform, whose signal is fed back to the power amplifier to form a closed-loop control for the vibrating amplitude and frequency.

The depth d of the water at rest is 5.0 cm. Surfactants, which can reduce the interfacial tension between two liquids or between a liquid and a solid [49,59], have significant effects on properties of the dynamics of surface waves [60,61]. Several drops of surfactants, e.g., Kodak Photo-Flo [38,59], are then added to minimize the surface pinning effect at the walls and reduce the surface tension, such that the boundaries of the surface may be regarded as moving freely and the eigenmodes of the Laplacian operator are approximately cosine functions. The tank is fixed on a vibration table, which vibrates harmonically in the vertical direction.

The whole setup of our experiment is shown in Fig. 1. It consists of a vibration unit (DongLing Vibration ES-3-150/LT0404, with the signal-to-noise ratio greater than 100 dB and frequency resolution equal to 0.1%), whose vibrator is driven by a power amplifier which can output amplified harmonic signals. The system has a closed-loop control regarding the amplitude and the frequency of the vibrator, where the power amplifier receives a feedback signal from an accelerometer that fixed on the vibrator; therefore the amplitude and the frequency of the vibrator can be fixed to the input value with high precision. A computer is used to set up parameters for the vibration unit to specify the starting amplitude or frequency, the step, the ending amplitude or frequency, and the duration of each step. In the beginning of the experiment, a laser range finder (Keyence IL-S025) is also used to measure the amplitude and frequency of the vibrator, which agree with the input values well, and the relative errors in A and f are 1.2% and 0.09%, respectively (see Supplemental Material [62]). It is important to know the level of horizontal vibration in the setup for parameters and payloads that we have used in the experiments, as the electromagnetic shakers possess such off-axis vibrations that could lead to spurious conclusions [63]. Therefore, we have measured the horizontal vibration using the laser range finder, and find that the amplitudes are around 6.5×10^{-5} cm in both x and y directions, which is about two orders smaller than the vertical driven amplitude $A = 0.018$ cm. It is known that while the vertical force plays the role of parametrically driving (exponential instability), the horizontal force plays the role of externally driving (linear instability) [13]. Taking mode (12,0)

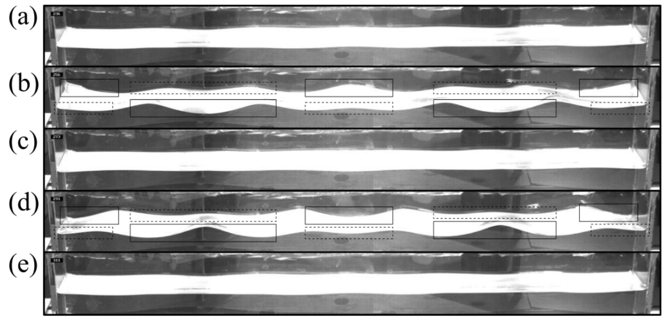

FIG. 2. The snapshots of the ALFW pattern in a period of oscillation. From (a) to (e) are the wave profiles with phase 0, $\frac{\pi}{2}$, π, $\frac{3\pi}{2}$, 2π, respectively. Regions in dashed boxes are almost flat all the time, while the regions in solid boxes oscillate with significant amplitudes; see (b) and (d). The driving frequency is $f = 8.66$ Hz and the driving amplitude is $A = 0.018$ cm, which are representative parameters for this phenomenon to occur.

for instance and taking the dissipation and horizontal force into consideration, one can obtain that the contribution of the horizontal force to the amplitude of the surface wave [13] is around 2.4×10^{-5} cm, which can be neglected in our case.

A water tank with length $L = 50$ cm and width $b = 5.5$ cm is fixed on the vibrator. It is partially filled with water where the height at rest is $d = 5.0$ cm. It is known that the dominant source of dissipation results from surface contamination that occurs fairly rapidly if the container is open to air; thus in our experiment, to reduce dissipation from surface contamination, the tank is covered right after adding water and surfactants. A high-speed CMOS camera (Basler-acA2040-180 km, 180 fps at 2048×2048 resolution) is placed in front of the tank to record the front side profile of the water surface. We extract the pixel data of the outline of the surface profile on the front side. Perspective correction is applied to this pixel data; after that the data are rescaled to actual values to yield the profile $\eta(x, y = 0)$. Discrete cosine transformation (DCT) is applied along the x direction to obtain its DCT spectra η_m.

B. Experimental phenomenon

In this subsection, we will first give a description of the basic features of the ALFW pattern, and then elucidate how the pattern is developed.

In order to characterize the pattern, we extract the wave profile at steady state from the captured video. Figures 2(a)–2(e) show the profiles of the ALFW pattern at phase stages 0, $\frac{\pi}{2}$, π, $\frac{3\pi}{2}$, 2π in one period of oscillation. Since the eigenmodes of the system are approximately cosine functions, the DCT would be a natural choice to perform spectral analysis, with its transformation coefficients being precisely the height of each normalized mode.

We find from the captured profiles the following:

(i) One of the important features of the pattern is that there are as many as five spatially localized regions with large oscillations, separated by flat regions that almost do not move during the oscillation. The localized region and the flat region appear alternately in both x and y directions (Fig. 2). In particular, in the y direction, if there is a localized region with large oscillations on the front side, it will be flat at the rest level on the opposite side all the time, forming a strong contrast, and vice versa. For example, the corners at the front side are flat regions that barely move during the oscillation, while the back corners belong to the localized region, which oscillates wildly. This is in contrast with most previously reported localized surface wave patterns, which are either one packet waves (e.g., the standing soliton [38]) or a series of packets only distributed along the x direction.

(ii) By the DCT of the front side of the surface profile (Fig. 3), it is found that although the localized pattern of the water surface wave is complicated, the components of its spectrum are

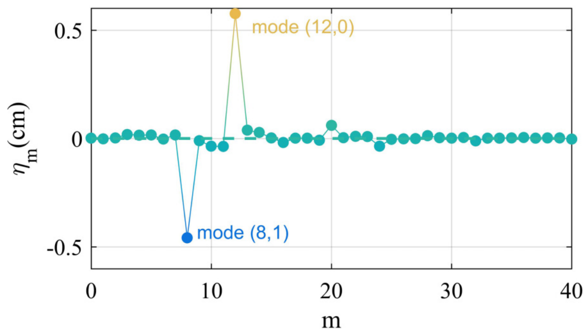

FIG. 3. The DCT spectrum of the front side ($y = 0$) of the surface profile shown in Fig. 2(b). It is clear that two clean modes, (8,1) and (12,0), dominate, with an opposite sign of their values.

rather simple: just two natural modes, (12,0) and (8,1), dominate. This result violates our intuition at first glance. Here, we would like to emphasize that although the spectrum of the pattern is rather simple, the pattern does not trivially result from the two *linearly* superposed counterpropagative natural modes.

Note that from the DCT of $\eta(x, 0)$, only the mode number m in the x direction can be determined, such as 12 or 8, while the mode number n in the y direction (0 or 1) cannot be fixed directly. In our case, n is determined by comparing the derived profile (Fig. 4) with the experimentally obtained surface wave.

(iii) The third feature of the ALFW pattern is robustness. We have repeated the experiments several times under each set of driving parameters; the pattern always emerges and oscillates at the same angular frequency, which implies the independence of the pattern on initial conditions. Furthermore, the phenomenon is stable to parameter variations as it appears in a finite region in the parameter space.

Interestingly, the DCT coefficients of the dominant modes have opposite sign, which indicates that the relative phase between these two modes is between $\pi/2$ and $3\pi/2$. When the relative phase between modes (12,0) and (8,1) is close to 0 or π, the peaks of the ALFW pattern achieve the maximum and the flat regions achieve their minimum. By artificially adjusting the relative phase between the dominant modes (8,1) and (12,0) to be π, we reproduce the ALFW pattern, as sketched in Fig. 4. In fact, the phase of mode (12,0) is always in advance of that of mode

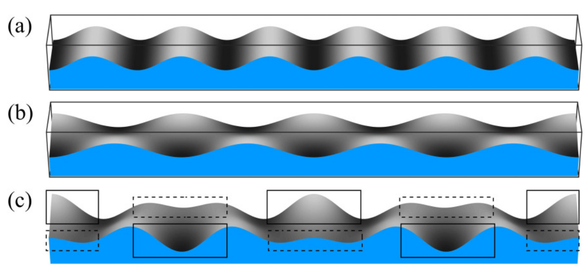

FIG. 4. The illustration of constructing the ALFW pattern by phenomenologically superposing the (12,0) and (8,1) modes. (a) Mode (12,0), (b) mode (8,1), and (c) superposition of the two modes with equal weights but opposite signs. Both large oscillation regions (enclosed by solid boxes) and the flat regions (enclosed by dashed boxes) are clearly seen. Note that our observed ALFW phenomenon is not only a linear superposition of the two modes, as they have different eigenfrequencies. Actually, the nonlinear interaction between these two modes locks their relative phase, finally resulting in the ALFW pattern.

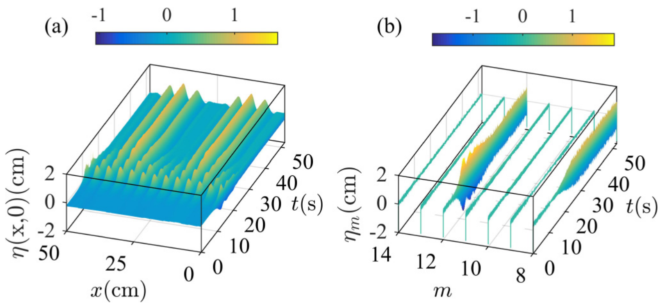

FIG. 5. The evolution of the ALFW pattern in (a) real space and (b) mode space. The driven parameters are $A = 0.04$ cm, $f = 8.64$ Hz. (a) Shows the time series of the profile η on one side of the tank ($y = 0$ cm, the front side of the profiles in Fig. 2). (b) Shows the time series of the DCT coefficients for the relevant modes in the x direction. The (12,0) mode is excited around $t = 10$ s, the (8,1) mode is developed around $t = 20$ s, and the system reaches a steady state around $t = 30$ s, forming the ALFW pattern. The coefficients of all the other modes remain close to 0.

(8,1) by approximately π, as we will demonstrate in Sec. VI (Fig. 9). This indicates that the phases of these two modes are locked. The eigenfrequencies of these two modes differ slightly. Without considering dissipation, the frequencies of modes (12,0) and (8,1) are 8.6980/2 Hz and 8.7389/2 Hz, respectively; see Eq. (9). The linear stability analysis yields that these two modes are all unstable. If this is the case, their frequencies will be detuned to the same value due to the external driving, and the nonlinear interaction between the two modes will exert additional selection rules and reduce the number of possible phases, which may lead to robust phase locking. However, when taking dissipation into consideration, they are 8.6974/2 Hz and 8.7378/2 Hz; see Eq. (15). As we will show in Sec. IV B, with dissipation, mode (8,1) is no longer in the Faraday instability region [Fig. 7(b)]; thus its excitation and phase locking with mode (12,0) are actually due to the nonlinear driving from mode (12,0).

Now, we examine how this ALFW pattern is developed. At each time instance, we record the wave profile $\eta(x, y = 0, t)$ at the front boundary of the tank. Figure 5(a) shows the time evolution of this profile. In the meantime, at each time instance, we do the DCT to $\eta(x, 0, t)$ with respect to x, and get the spectrum of the amplitudes $\eta_m(t)$ in the mode space. The results are shown in Fig. 5(b). It is clear from the time series of the profile and the DCT spectrum that after turning on the vibrator at $t = 0$, a transient time lasts about ten seconds, where the water surface is almost static. As the fluctuations of the surface enhance, a standing wave of a single mode with wave number $k_{12,0}$ emerges, which indicates the excitation of mode (12,0). After the standing wave being established and the amplitude exceeds some threshold, at around $t = 20$ s, the mode (8,1) is also excited, and gradually the amplitudes of these two modes become stable, where the ALFW profile is formed. Over the whole stage, the coefficients of all the other modes remain close to 0. These features reveal how the ALFW pattern is formed.

We have also examined the water surface wave with different driving parameters. For example, we fix the driving amplitude at 0.018 cm and vary the driving frequency systematically. The representative snapshots are plotted in Fig. 6. When the driving frequency f is in the range of [8.68, 8.76] Hz, only the (12,0) mode is excited; if f is in the range of [8.64, 8.67] Hz, then both (12,0) and (8,1) modes can be excited, and the ALFW pattern is formed. When the driving frequency is greater than 8.76 Hz or smaller than 8.64 Hz, and the driving amplitude is at 0.018 cm, none of the modes are in the unstable region; thus the water surface remains static. Therefore, there is a region in the parameter space of the driving frequency and the driving amplitude where the pattern can emerge. The boundary of this region in the parameter space can be determined by nonlinear competition theory, as developed in Sec. V, which agrees with the experimental results well [see Fig. 8(a)].

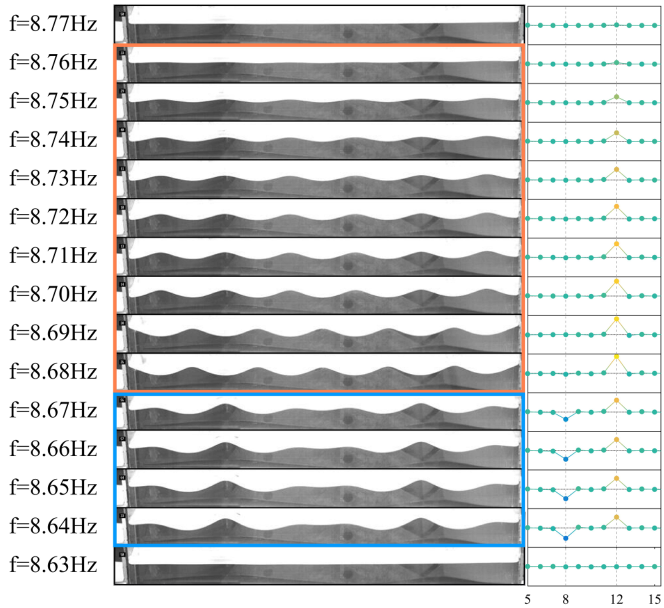

FIG. 6. Representative water surface profiles at the front boundary when the system is steady and the amplitude is at its maximum. The driving amplitude is fixed to 0.018 cm. From top to bottom the frequencies are 8.77 Hz to 8.63 Hz with a decreasing step of 0.01 Hz. If the driving frequency is greater than 8.76 Hz or smaller than 8.64 Hz, the water surface cannot be excited at the given driving amplitude. There is an abrupt change in the dominant modes between 8.68 Hz and 8.67 Hz. If the driving frequency f is in the range of [8.68, 8.76] Hz (enclosed by the orange rectangle), only the (12,0) mode is excited; if f is in the range of [8.64, 8.67] Hz (enclosed by the sky blue rectangle), then both (12,0) and (8,1) modes can be excited, and the ALFW pattern is formed. Note that the profile for $f = 8.68$ Hz and 8.69 Hz is the same for the upper ones but with a π phase difference.

III. GOVERNING EQUATIONS AND BOUNDARY CONDITIONS OF GRAVITY WATER SURFACE WAVES

In this section we provide briefly the basics of mathematical models of water surface waves, based on which further analysis will be carried out. The starting point is the Navier-Stokes equation

$$\frac{\partial \boldsymbol{u}}{\partial t} + (\boldsymbol{u} \cdot \nabla)\boldsymbol{u} = \rho \boldsymbol{g} - \nabla p + \mu \nabla^2 \boldsymbol{u}, \tag{1}$$

where $\boldsymbol{u} = \boldsymbol{u}(x, y, z)$ is the three-dimensional velocity field, ρ is the density of water, $\boldsymbol{g}$ is the gravity constant, p is the pressure, and μ is the viscous factor. Typical values of the parameters in our experiment are given in Table I.

TABLE I. Typical values of parameters in our experiment.

Symbol	Value
Length of x domain, L (cm)	50.0
Surface tension, γ (dyn/cm)	20.0
Length of y domain, b (cm)	5.5
Density of water, ρ (g/cm^3)	1.0
Mean depth in the z direction, d (cm)	5.0
Gravity constant, g (cm/s^2)	981

To formulate our model, we fix the coordinate on the tank (Fig. 1). The linearized effects of the surface tension $\gamma\nabla^2\eta/\rho\hat{z}$ (see [49,52]) on the free surface $z=\eta(x,y,t)$ and the effects of harmonic driving force $\boldsymbol{I}\cos\omega t$ are incorporated into the gravity parameter $\boldsymbol{g}$, where $\boldsymbol{I}=\hat{z}A\omega^2$; A and $\omega=2\pi f$ are the driving amplitude and the driving angular frequency, respectively. The resulting effective gravity constant is $\tilde{\boldsymbol{g}}=\boldsymbol{g}+\gamma\nabla^2\eta/\rho\hat{z}+\boldsymbol{I}\cos\omega t$. Assuming that the water in the tank is irrotational, $\nabla\times\boldsymbol{u}(x,y,z)=0$, and incompressible, $\nabla\cdot\boldsymbol{u}(x,y,z)=0$, then the velocity potential $\phi(x,y,z,t)$ can be introduced as $\boldsymbol{u}(x,y,z)\equiv\nabla\phi(x,y,z)$, which satisfies the Laplacian equation

$$\nabla^2\phi(x,y,z)=0. \tag{2}$$

Neglecting the bulk dissipation provisionally, Eq. (1) can be reduced to the Bernoulli equation

$$\frac{\partial\phi}{\partial t}+\frac{1}{2}(\nabla\phi)^2+\tilde{g}z+\frac{p-p_0}{\rho}=0, \tag{3}$$

where p_0 is the pressure of atmosphere on the water surface. A moderate amount of additive (Kodak Photo-Flo) is added into the water to minimize the effects of surface tension [38], such that the boundaries of the contact line satisfy, approximately, the homogeneous Neumann boundary conditions,

$$\left.\frac{\partial\eta(x,y,t)}{\partial x}\right|_{y=0,b}\approx 0,\qquad \left.\frac{\partial\eta(x,y,t)}{\partial y}\right|_{x=0,L}\approx 0. \tag{4}$$

The no-penetration boundary conditions on the wall and at the bottom read

$$\hat{\boldsymbol{n}}\cdot\nabla\phi(x,y,z,t)=0,\ (x,y,z)\in\partial V, \tag{5}$$

where $\hat{\boldsymbol{n}}$ is the unit normal vector at the wall. The dynamical equation [Eq. (3)] on the surface $z=\eta(x,y,t)$ and the requirement of the free surface $\eta(x,y,t)$ give the dynamical and kinetic boundary conditions, respectively:

$$\frac{\partial\phi}{\partial t}+\frac{1}{2}(\nabla\phi)^2+\tilde{g}\eta=0,\quad z=\eta, \tag{6a}$$

$$\frac{\partial\eta}{\partial t}+\nabla\phi\cdot\nabla\eta=\frac{\partial\phi}{\partial z},\quad z=\eta. \tag{6b}$$

IV. LINEAR ANALYSIS

A. Linear approximations

In order to perform stability analysis of the system, we adopt the Lagrangian form derived in [13]. Because of the homogeneous Neumann boundary conditions (4) of the water surface $z=\eta(x,y,t)$ at the walls, the surface wave can be expanded by cosine function basis $\psi_{mn}(x,y)=\cos k_m x\cos k_n y$:

$$\eta(x,y,t)=\eta_{mn}(t)\cos k_m x\cos k_n y, \tag{7}$$

where the wave numbers are $k_m=m\pi/L, k_n=n\pi/b$. The satisfaction of both the Laplacian equation [Eq. (2)] and the no-penetration boundary conditions Eq. (5) of the velocity potential $\phi(x,y,z,t)$ leads to the expansion:

$$\phi(x,y,z,t)=\phi_{mn}(t)\cosh k_{mn}(z+d)\cos k_m x\cos k_n y, \tag{8}$$

where $k_{mn}^2=k_m^2+k_n^2$. The dispersion relation between the natural angular frequency ω_{mn} and the corresponding wave vector k_{mn} can be obtained by dropping the nonlinear terms of Eq. (6):

$$\omega_{mn}^2\simeq\left(g+\gamma\frac{k_{mn}^2}{\rho}\right)k_{mn}\tanh(k_{mn}d). \tag{9}$$

The first term is due to gravity, and second term is due to the surface tension. For the relevant modes considered in this paper and the estimated value of γ from the experimental data (Sec. VI), the relative weight of the surface tension over the gravity is about 1% (see Supplemental Material [64]). Even for pure water with maximum surface tension [65], the relative weight is still only around 4%. Although surface tension may have observable effects, it is far from being comparable to the gravity effect. Therefore the dynamical phenomena observed in our experiments are mainly gravity surface waves.

The Lagrangian of the system is

$$L = (\rho S)^{-1}(T - V) = \sum_{m,n,m',n'=0}^{\infty} \left(\frac{1}{2} a_{m'n',mn} \frac{\partial \eta_{mn}}{\partial t} \frac{\partial \eta_{m'n'}}{\partial t} - \frac{1}{2} \tilde{g} \eta_{mn} \eta_{mn} \right),$$

where $S = L \times b$ is the cross area of the tank. The nonlinear inertial coefficients $\boldsymbol{a} \equiv \{a_{m'n',mn}\}$, in the small slope limit, can be expanded in series of generalized coordinates η_{mn},

$$\begin{aligned} a_{m'n',mn} = \delta_{mm'}\delta_{nn'}a_{m'n'} &+ \sum_{m'',n''=0} a_{m''n'',m'n',mn}\eta_{m''n''} \\ &+ \frac{1}{2}\sum_{m''',n'''=0} a_{m'''n''',m''n'',m'n',mn}\eta_{m'''n'''}\eta_{m''n''} + \cdots , \end{aligned} \tag{10}$$

where

$$a_{mn} = k_{mn}^{-1} \tanh^{-1}(k_{mn}d) \simeq \left(g + \gamma \frac{k_{mn}^2}{\rho} \right) \omega_{mn}^{-2} \tag{11}$$

is the linear part of the inertia; $a_{m''n'',m'n',mn}$, $a_{m'''n''',m''n'',m'n',mn}, \ldots$ are the nonlinear coupling coefficients of the first order, the second order, etc., respectively.

Dropping terms of order $O(\eta)$ in Eq. (10), we obtain the linearized Lagrangian

$$L_0 = \sum_{m,n=0}^{\infty} \left(\frac{1}{2} a_{mn} \frac{\partial \eta_{mn}}{\partial t} \frac{\partial \eta_{mn}}{\partial t} - \frac{1}{2} \tilde{g} \eta_{mn} \eta_{mn} \right). \tag{12}$$

B. Parametric instability analysis

Substituting the linear inertia [Eq. (11)] into the linearized Lagrangian [Eq. (12)], and employing the Euler-Lagrange equations, one can obtain a set of Mathieu equations for each mode (m, n):

$$\frac{d^2 \eta_{mn}}{dt^2} + \left(\omega_{mn}^2 + I_{mn} \cos \omega t\right)\eta_{mn} = 0, \tag{13}$$

where $I_{mn} = k_{mn} \tanh(k_{mn}d) A\omega^2$; A and ω are the driving amplitude and the driving angular frequency. Here the fluid is provisionally assumed to be inviscid (no dissipation). However, in a realistic case, dissipation is inevitable, which will change both the parameter values and the boundary of the instability region. Adding the dissipation term $\mu_{m,n}\dot{\eta}_{m,n}$ to the left of Eq. (13), where μ_{mn} is the dissipation rate, and taking the transformation

$$\eta_{mn} = \xi_{mn} \exp\left(-\mu_{mn} t/2\right), \tag{14}$$

we will have the natural frequencies $\Omega_{m,n}$ that incorporate the dissipation effect

$$\Omega_{m,n}^2 = \omega_{m,n}^2 - \frac{\mu_{m,n}^2}{4}. \tag{15}$$

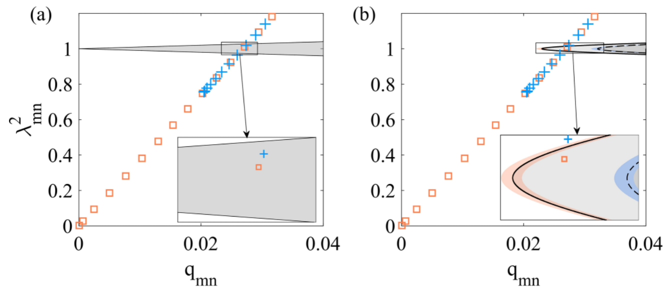

FIG. 7. For fixed driven parameters $A = 0.018$ cm and $f = 8.66$ Hz, the stability phase diagram of the Mathieu equation [Eq. (16)] (a) without and (b) with dissipation. The orange squares are the parameter values for the 0 modes, and the blue plus symbols are those for the 1 modes in the y direction. (a) The gray region indicates the unstable phase without dissipation. (b) The light orange and gray areas are the unstable regions with dissipation 0.625 s^{-1} [for mode (12,0)] and 0.873 s^{-1} [for mode (8,1) when it is excited solely], respectively. It shows that in (a) by assuming the inviscid condition in our experiment, both modes (12,0) and (8,1) fall in the gray unstable region, while in (b) with the dissipation (see text), the unstable region shrinks and mode (8,1) is no longer unstable. Inset of (b) shows the zoom-in of the tip of the unstable region, with light orange and blue shaded areas being the boundary with the maximum uncertainty in dissipation. The outer and inner outlines of the light orange area covering the solid curve correspond to $\mu_{12,0} = 0.6$ and 0.645 s^{-1}, and the outer and inner outlines of the blue area covering the dashed curve correspond to $\mu_{8,1} = 0.845, 0.887$ s^{-1}, respectively, which demonstrate clearly that mode (12,0) is unstable and mode (8,1) is stable, and the results are robust with maximum uncertainties in key coefficient estimations.

By rescaling the time as $\tau = \omega t/2$, we can write Eq. (13) in the form of the standard Mathieu equation [52]

$$\frac{d^2\xi_{mn}}{d\tau^2} + (\lambda^2_{mn} + 2q_{mn}\cos 2\tau)\xi_{mn} = 0, \tag{16}$$

where $\lambda^2_{mn} = 4\Omega^2_{m,n}/\omega^2$ and $q_{mn} = 2Ak_{mn}\tanh(k_{mn}d)$. In fact, the dissipation term μ^2_{mn} in the formula of λ^2_{mn} is much smaller than the term $4\omega^2_{mn}$, so that it can be neglected. Thus the effect of dissipation μ_{mn} on the instability region is mainly reflected in its exponential factor in the transformation Eq. (14). Actually, the dissipation effects will reduce the area of the instability region.

In Fig. 7, the subharmonic unstable region of the Mathieu equation is painted in the shaded area, and the corresponding parameter values of the 0 and 1 modes in the y direction are plotted. Figure 7(a) is for the inviscid case ($\mu_{mn} = 0$), while Fig. 7(b) is with dissipation. From the well-known results of the Mathieu equation, mode ξ_{mn} is exponentially unstable if the corresponding parameter pair (q_{mn}, λ^2_{mn}) falls in the unstable region in the phase space, and then it can be observed in experiments. Note that Fig. 7 is the instability space of the linearized system and is applicable only for Faraday waves in the stage when their amplitudes are small. So only the linear coefficients, γ and $\mu_{m,n}$, are relevant. To be concrete, the dissipation rates of modes (12,0) and (8,1) can be estimated by fitting the instability curves [54], which are approximately 0.625 s^{-1} and 0.873 s^{-1} for modes (12,0) and (8,1), respectively. Note that for mode (8,1), the dissipation is obtained from the instability boundary where it is the only unstable mode for subharmonic response, which is different from that shown in Fig. 8, where mode (8,1) is unstable mainly due to the driving by mode (12,0); otherwise it will be stable in that parameter region.

In the inviscid case, when the driving amplitude and frequency are $A = 0.018$ cm and $f = 8.66$ Hz, for instance, there are two modes (12,0) and (8,1) that fall in the unstable region [Fig. 7(a)]. However, when a proper dissipation is introduced in the model to fit with the experiments, the unstable region shrinks and mode (8,1) has been kicked out; only mode (12,0) still resides in the

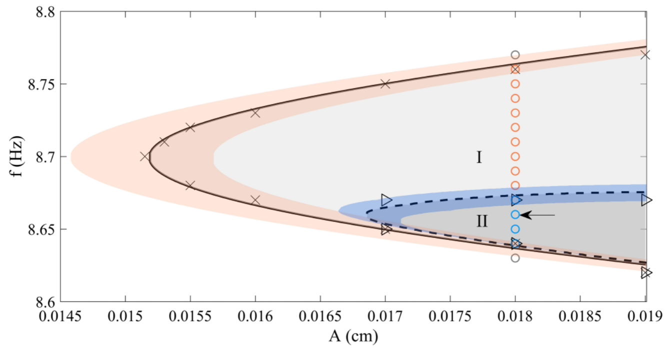

FIG. 8. The phase diagram in the driven parameter space. The crosses and triangles are the instability boundaries obtained experimentally for modes (12,0) and (8,1), respectively. The solid and dashed curves are fittings from our model (22). The adopted parameters are $\gamma = 20$ dyn/cm, and $\mu_{12,0} = 0.625\ \mathrm{s}^{-1}$, $\mu_{8,1} = 0.65\ \mathrm{s}^{-1}$, $\alpha_{8,1} = -1100/I_{8,1}$. The unstable regions for modes (12,0) and (8,1) are marked by I and II, respectively. Note that in region II, mode (12,0) is also unstable; thus region II is for the ALFW phenomenon. The driving amplitude and frequency we used for most of the results in the paper, $A = 0.018$ cm and $f = 8.66$ Hz, is marked by an arrow in region II. The circles indicate the parameter values in Fig. 6. The gray circles are outside the unstable region, the orange circles are where only mode (12,0) is unstable, the blue circles are where both mode (12,0) and mode (8,1) are unstable. The corresponding uncertainty range for parameters γ, $\mu_{12,0}$ (light orange) and for parameters $\mu_{8,1}$, $\alpha_{8,1}$ (light blue) are also shown. The outer and inner outlines of the orange area covering the solid curve correspond to $\gamma = 20.1$ dyn/cm, $\mu_{12,0} = 0.6\ \mathrm{s}^{-1}$ and $\gamma = 19.65$ dyn/cm, $\mu_{12,0} = 0.645\ \mathrm{s}^{-1}$, respectively. The outer and inner outlines of the blue area covering the dashed curve correspond to $\mu_{8,1} = 0.64\ \mathrm{s}^{-1}$, $\alpha_{8,1} = -1000 I_{8,1}^{-1}$ and $\mu_{8,1} = 0.66\ \mathrm{s}^{-1}$, $\alpha_{8,1} = -1200 I_{8,1}^{-1}$, respectively.

unstable region [Fig. 7(b)]. Note that uncertainties of the fitted coefficients are estimated and even with the maximum uncertainty, the results are still robust; i.e., mode (12,0) is unstable and mode (8,1) is stable. However, since both modes (12,0) and (8,1) are prominent in the DCT spectrum (Fig. 3), the observed (8,1) mode in our experiments must be excited by mode (12,0) through the nonlinear interactions, which will be analyzed in detail in Sec. V.

V. NONLINEAR MODEL IN THE UNSTABLE SUBSPACE

In light of the DCT spectrum of the surface pattern, we consider the subspace spanned by the two dominant modes (12,0) and (8,1). The surface profile can be written in terms of the corresponding coefficients $\eta_{12,0}$ and $\eta_{8,1}$,

$$\eta(x, y, t) = \eta_{12,0}(t)\cos(k_{12}x)\cos(k_0 y) + \eta_{8,1}(t)\cos(k_8 x)\cos(k_1 y), \tag{17}$$

and the reduced Lagrangian (without dissipation) can be written as

$$\begin{aligned} L_{\mathrm{sub}} = {} & \tfrac{1}{2}a_{12,0;12,0}\dot{\eta}_{12,0}^2 + \tfrac{1}{2}a_{8,1;12,0}\dot{\eta}_{8,1}\dot{\eta}_{12,0} + \tfrac{1}{2}a_{12,0;8,1}\dot{\eta}_{12,0}\dot{\eta}_{8,1} + \tfrac{1}{2}a_{8,1;8,1}\dot{\eta}_{8,1}^2 \\ & - \tfrac{1}{2}(g - I\cos\omega t)\eta_{12,0}^2 - \tfrac{1}{2}(g - I\cos\omega t)\eta_{8,1}^2. \end{aligned} \tag{18}$$

The nonlinearity arises from the nonlinear inertia $a_{m'n',mn}$, which depends on η. In the unstable subspace, it is easy to calculate the coupling overlaps $a_{12,0;12,0} = a_{12,0}[1 - 4k_{12}^2(\eta_{12,0}^2 + \eta_{8,1}^2)] + \cdots$, $a_{8,1;12,0} = 0$, $a_{12,0;8,1} = 0$, $a_{8,1;8,1} = a_{8,1}[1 - 4k_{8,1}^2(\eta_{12,0}^2 + \frac{3}{8}\eta_{8,1}^2)] + \cdots$.

Substituting L_{sub} into the Euler-Lagrange equations and neglecting the terms of order $O(\eta^4)$, we obtain the corresponding second-order ODEs in the four-dimensional unstable subspace:

$$\begin{aligned}
&\frac{d^2\eta_{12,0}}{dt^2} + \{\omega_{12,0}^2 - I_{12,0}[1 + 4k_{12,0}^2(\eta_{12,0}^2 + \eta_{8,1}^2)]\cos\omega t\}\eta_{12,0} \\
&\quad = k_{12,0}\tanh(k_{12,0}d)[4\eta_{12,0}(k_{12,0}\dot{\eta}_{12,0}^2 - k_{8,1}\dot{\eta}_{8,1}^2) + 8k_{12,0}\eta_{8,1}\dot{\eta}_{8,1}\dot{\eta}_{12,0}] \\
&\qquad - 4\omega_{12,0}^2 k_{12,0}(\eta_{12,0}^2 + \eta_{8,1}^2)\eta_{12,0}, \qquad (19a)\\
&\frac{d^2\eta_{8,1}}{dt^2} + \{\omega_{8,1}^2 - I_{8,1}[1 + 4k_{8,1}^2(\eta_{12,0}^2 + 3\eta_{8,1}^2/8)]\cos\omega t\}\eta_{8,1} \\
&\quad = k_{8,1}\tanh(k_{8,1}d)[\eta_{8,1}(-4k_{12,0}\dot{\eta}_{12,0}^2 + 3k_{8,1}\dot{\eta}_{8,1}^2/2) + 8k_{8,1}\eta_{12,0}\dot{\eta}_{12,0}\dot{\eta}_{8,1}] \\
&\qquad - 4\omega_{8,1}^2 k_{8,1}(\eta_{12,0}^2 + 3\eta_{8,1}^2/8)\eta_{8,1}. \qquad (19b)
\end{aligned}$$

The coupling terms between the two dominant modes appear naturally.

Phenomenological strong nonlinear model

It is interesting to find that the structure of the above two cubic nonlinear equations resemble the mode competition equations used by Gollub *et al.* [54]. Both quadratic "parametric coupling" and cubic nonlinear terms appear. The above equations can be further simplified to a phenomenological model based on certain physical considerations. First, the resonant coupling terms $\eta_{8,1}^2\eta_{12,0}\cos\omega t$ in the equation of $\eta_{12,0}$ and $\eta_{12,0}^2\eta_{8,1}\cos\omega t$ in the equation of $\eta_{8,1}$ should be kept to account for the internal mode interactions. Second, the other nonlinear terms can be neglected, but the self-cubic terms are retained to keep the system bounded [48], which can be combined as $\beta_{12,0}\eta_{12,0}^3$ and $\beta_{8,1}\eta_{8,1}^3$. Therefore, letting $\alpha_{12,0}$ and $\alpha_{8,1}$ be the coefficients for the resonant coupling terms, we obtain

$$\ddot{\eta}_{12,0} + [\omega_{12,0}^2 - I_{12,0}(1 + \alpha_{12,0}\eta_{8,1}^2)\cos\omega t]\eta_{12,0} = \beta_{12,0}\eta_{12,0}^3 \qquad (20)$$

and

$$\ddot{\eta}_{8,1} + [\omega_{8,1}^2 - I_{8,1}(1 + \alpha_{8,1}\eta_{12,0}^2)\cos\omega t]\eta_{8,1} = \beta_{8,1}\eta_{8,1}^3. \qquad (21)$$

Taking the dissipation effects back into consideration, we have

$$\ddot{\eta}_{12,0} + \mu_{12,0}\dot{\eta}_{12,0} + [\omega_{12,0}^2 - I_{12,0}(1 + \alpha_{12,0}\eta_{8,1}^2)\cos\omega t]\eta_{12,0} = \beta_{12,0}\eta_{12,0}^3, \qquad (22a)$$

$$\ddot{\eta}_{8,1} + \mu_{8,1}\dot{\eta}_{8,1} + [\omega_{8,1}^2 - I_{8,1}(1 + \alpha_{8,1}\eta_{12,0}^2)\cos\omega t]\eta_{8,1} = \beta_{8,1}\eta_{8,1}^3. \qquad (22b)$$

Now we have the equations that are exactly the same as in [48,54].

VI. DETERMINATION OF THE KEY PARAMETERS AND UNCERTAINTY ANALYSIS

The unstable region can be obtained experimentally as follows. First, we discretized the parameter space with $\Delta A = 0.001$ cm and $\Delta f = 0.0125$ Hz. Then for each point (A, f) in the parameter space, we conducted the experiment and waited at most 10 minutes to see if any mode can be excited, as demonstrated in Fig. 6, then moved to the next parameter value. Due to the exponential divergency of the Mathieu instability, if there is an unstable mode, it will be excited quickly, typically within one minute. Thus 10 minutes are in general long enough to observe an excitation of the unstable modes if there are any. The criterion of excitation of a mode is judged by the DCT spectrum. Then the boundary of the unstable region can be obtained by setting a critical value of 0.1 cm. The results are shown in Fig. 8. From the mode coupling equations (22), for each set of the coefficients, the instability boundary in the parameter space (A, f) can be determined. Thus the key coefficients of the nonlinear model can be derived from the fitting to the experimentally obtained boundaries and the time series of the two dominating modes. The fitting coefficients of the nonlinear model are the surface tension γ, the dissipation rates $\mu_{12,0}$ and $\mu_{8,1}$, the coupling coefficients $\alpha_{12,0}$ and $\alpha_{8,1}$, and the cubic nonlinear coefficients $\beta_{12,0}$ and $\beta_{8,1}$. Since the instability boundary of the leading mode (12,0) is relatively independent and mostly relies on the values of γ and $\mu_{12,0}$, thus they can be determined first. The instability boundary of the passive mode (8,1) relies on γ, $\mu_{8,1}$, and also $\alpha_{8,1}$. Therefore $\mu_{8,1}$ and also $\alpha_{8,1}$ can be determined second. The cubic nonlinearity coefficients $\beta_{12,0}$, $\beta_{8,1}$ and the nonlinear modal coupling coefficient $\alpha_{12,0}$ jointly determine the height of the two modes' amplitudes and their relative phase, which can be determined third. According to the discussion above, the fitting of these parameters is carried out in three steps. Uncertainties of these coefficients and their effects are also analyzed.

A. Determination of γ and $\mu_{12,0}$

For the *weakly* dissipative Mathieu equation (whether linear or not), the dissipative coefficient $\mu_{m,n}$ can be, in principle, determined solely from the tip (the leftmost threshold in the parameter space) of the boundary curve [66,67]. This is true for mode (12,0), because there exists a region in the parameter space containing a tip where only mode (12,0) is excited. However, this is not the case for mode (8,1), as the tip of the instability boundary for mode (8,1) is covered by the unstable region for mode (12,0).

The dissipative coefficient can be estimated from experimental data via the formula $\mu_{m,n} \simeq \omega^* q^*_{m,n}/4$, where the star indicates quantities at the tip of the instability region [66,67]. For mode (12,0), it is

$$\mu_{12,0} \simeq \frac{\omega^* I^*_{12,0}}{4\omega^2_{12,0}} = \frac{\omega^{*3} k_{12,0} \tanh(k_{12,0} d) A^*}{4 g k_{12,0} \tanh(k_{12,0} d)} = \frac{\omega^{*3} A^*}{4g}. \tag{23}$$

On the other hand, it is known that the driven angular frequency at the tip (subharmonic) is twice the natural frequency of the instability mode. For mode (12,0), we have

$$\omega^* = 2\left[\left(g + \gamma \frac{k^2_{m,n}}{\rho}\right) k_{m,n} \tanh(k_{m,n} d)\right]^{1/2}. \tag{24}$$

Therefore we can fit $(\mu_{12,0}, \gamma)$ with the tip of the experimentally obtained instability boundary, e.g., $(\omega^*, A^*) = (2\pi \times 8.7\ \text{rad/s}, 0.0151\ \text{cm})$, as shown in Fig. 8. As such, we obtain the surface tension $\gamma = 20$ dyn/cm, and the dissipative coefficient $\mu_{12,0} = 0.625\ \text{s}^{-1}$ as our best fit.

Note that for the standard dimensionless dissipative Mathieu equation $\ddot{x} + \mu \dot{x} + [1 + h\cos(2+\epsilon)t]x = 0$, close to the tip of the subharmonic instability boundary, i.e., $\epsilon \ll 1$ and $h \ll 1$, the instability condition is given by

$$-\sqrt{\left(\tfrac{1}{2}h\right)^2 - 4\mu^2} < \epsilon < \sqrt{\left(\tfrac{1}{2}h\right)^2 - 4\mu^2}, \tag{25}$$

where $h > 4\mu$. Thus the weakly damping condition is given by $\mu < h/4 \ll 1$. For mode (m, n), $\mu = \mu_{m,n}/\omega_{m,n}$. In our experiments, for mode (12,0), we have $\mu = \mu_{12,0}/\omega_{12,0} = 0.0229$, which is much less than one and justifies the weak dissipation condition.

The uncertainties for parameters $\gamma, \mu_{12,0}$ (the orange region in Fig. 8) can be estimated as follows. The outer and inner outlines of the orange region indicate the minimum variation to the parameter $\gamma, \mu_{12,0}$ to cover all the data on the instability boundary. In particular, the outer and inner outlines correspond to $\gamma = 20.1$ dyn/cm, $\mu_{12,0} = 0.6\ \text{s}^{-1}$ and $\gamma = 19.65$ dyn/cm, $\mu_{12,0} = 0.645\ \text{s}^{-1}$, respectively. For any parameter p, we define the relative uncertainty as

$$u = \frac{|p_{\max} - p_{\min}|}{2p_0}, \tag{26}$$

where p_0 is the fitted value. So the relative uncertainties for γ and $\mu_{12,0}$ are $u_\gamma = 1.13\%$ and $u_{\mu_{12,0}} = 3.6\%$, respectively.

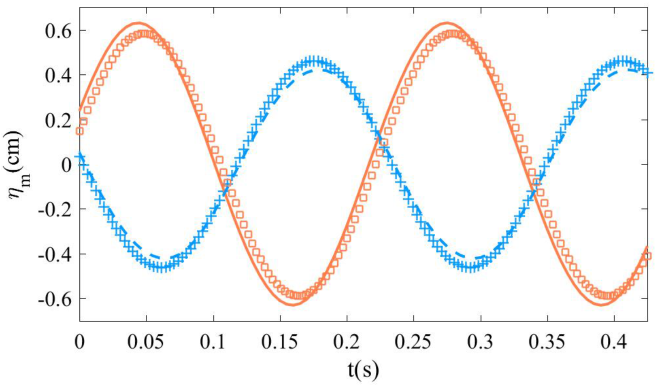

FIG. 9. Comparison of the simulated asymptotic trajectories (the curves) and the experimental data (the symbols) with driven parameters $A = 0.018$ cm and $f = 8.66$ Hz. The solid curve and the squares are for mode (12,0), while the dashed curve and the plus symbols are for mode (8,1). In our simulations, the coefficients in Eq. (22) are $\mu_{12,0} = 0.625\ \mathrm{s}^{-1}$, $\alpha_{12,0} = 150/I_{12,0}$, $\beta_{12,0} = 100\ \mathrm{cm}^{-2}\ \mathrm{s}^{-2}$, $\mu_{8,1} = 0.65\ \mathrm{s}^{-1}$, $\alpha_{8,1} = -1100/I_{8,1}$, $\beta_{8,1} = -800\ \mathrm{cm}^{-2}\ \mathrm{s}^{-2}$, and the initial condition is $\eta_{12,0} = 0.01$ cm, $\eta_{8,1} = 0$ cm, and $\dot{\eta}_{m,n} = 0$ cm/s. The magnitude of the initial fluctuation is 0.01 cm. The amplitudes, frequencies, and relative phase between the two dominant modes (12,0) and (8,1) approach constant values asymptotically. The relative phase is always a little more than π, which shows the phase locking between the two dominant modes due to the nonlinear coupling, and also enhances the coherence and stability of the ALFW profile of the observed surface waves.

B. Determination of $\mu_{8,1}$ and $\alpha_{8,1}$

The relative uncertainties for parameters $\mu_{8,1}$ and $\alpha_{8,1}$ can be obtained similarly as shown in the blue region in Fig. 8. The best fit to the data yields $\mu_{8,1} = 0.65\ \mathrm{s}^{-1}$, $\alpha_{8,1} = -1100 I_{8,1}^{-1}$. The outer and inner outlines of the blue region, to cover all the data points, correspond to $\mu_{8,1} = 0.64\ \mathrm{s}^{-1}$, $\alpha_{8,1} = -1000 I_{8,1}^{-1}$ and $\mu_{8,1} = 0.66\ \mathrm{s}^{-1}$, $\alpha_{8,1} = -1200 I_{8,1}^{-1}$, respectively. The relative uncertainties are then $u_{\mu_{8,1}} = 1.54\%$ and $u_{\alpha_{8,1}} = 9.09\%$, respectively.

It should be noted that for mode (8,1), the above dissipation is obtained by fitting to the instability boundary when mode (12,0) is also unstable, e.g., when the ALFW pattern is observed. Furthermore, since this is the case where the instability of mode (8,1) is due to the driving of mode (12,0), the obtained dissipation for the mode coupling model is different from that used in Fig. 7(b), where only mode (12,0) is unstable due to the subharmonic Mathieu instability.

C. Determination of $\beta_{12,0}$, $\beta_{8,1}$, and $\alpha_{12,0}$

The dissipation term in the Mathieu equations cannot bound the exponential growth of the amplitude to be finite; in fact, it is the nonlinear terms, i.e., $\beta_{12,0}$ and $\beta_{8,1}$, that bound the amplitude. In the meantime, the parameter $\alpha_{12,0}$ plays the role of feedback from the passive mode, so it may also affect the leading mode's amplitude. We can use the asymptotic amplitudes to determine the nonlinear factors $\beta_{12,0}$, $\beta_{8,1}$, and the feedback coupling $\alpha_{12,0}$.

In this framework, we choose a representative pair of parameters in phase space, e.g., $f = 8.66$ Hz, $A = 0.018$ cm. The detailed methodology is as follows. For each set of values for these three coefficients, the coupled ODEs (22) for the mode amplitudes are solved numerically by RK4 in the time domain with step $h = 0.005$ s, and the steady state solutions $\eta_{m,n}$ for modes (12,0) and (8,1) are obtained and compared with the time series obtained from experiments in Fig. 9. Since there are three coefficients, we fix two of the coefficients, and vary the remaining one (see Supplemental Material [68]). For example, we can fix $\beta_{8,1}$ and $\beta_{12,0}$, and vary $\alpha_{12,0}$. By comparing their amplitudes with that of the experimental data, we can obtain the amplitude difference for the two modes $\Delta\eta_{12,0}$ and $\Delta\eta_{8,1}$. This procedure can be carried out for the other two coefficients. After a few rounds, a set of optimal values for these three coefficients can be obtained, which are $\beta_{12,0} = 100\ \mathrm{cm}^{-2}\ \mathrm{s}^{-2}$, $\beta_{8,1} = -800\ \mathrm{cm}^{-2}\ \mathrm{s}^{-2}$, $\alpha_{12,0} = 150/I_{12,0}$. One can see from Fig. 9 that both the amplitudes and the relative phase agree well between the model Eq. (22) and the experimental results; in particular, the amplitude is bounded, and the phase of mode (12,0) is fixed to be in advance of the phase of mode (8,1) by a little more than π. This specific phase locking enhances the localization of amplitude in water surface waves, which is consistent with the observations in our experiments.

Since there may still be discrepancies between the theoretical model and the experiment, a complete simultaneous coincidence for both of the modes cannot be obtained. Thus with two coefficients taking the value from the set of optimal coefficients, varying the remaining one, there will be two values that each correspond to a better coincidence with one mode (see the Supplemental Material [68]). The difference between these two values can be regarded as the uncertainty for this parameter, e.g., for a coefficient p, $u = \Delta p/2p_0$. From the numerical results, we have $u_{\alpha_{12,0}} = 10\%$, $u_{\beta_{12,0}} = 4.3\%$, $u_{\beta_{8,1}} = 9.9\%$.

Since the experiment always starts from a nearly static state, i.e., $\eta_{m,n} \simeq 0$ and $\dot{\eta}_{m,n} \simeq 0$, in our simulation, the initial values for $\eta_{m,n}$ and $\dot{\eta}_{m,n}$ are small. In this regime, the excitation behavior of the system is mainly dominated by the Mathieu instability. Therefore, since mode (8,1) is in the linearly stable region, with the dissipation, $\eta_{8,1}$ will shrink quickly; while even there is dissipation, mode (12,0) lies in the unstable region, and thus $\eta_{12,0}$ will increase exponentially, until nonlinear effects take part such that $\eta_{12,0}$ can be bounded to a finite value. And when $\eta_{12,0}$ becomes large enough, the nonlinear interaction from mode (12,0) to mode (8,1) becomes dominant, making it unstable so that $\eta_{8,1}$ also increases to a finite value. Given this mechanism, insofar as the initial values are small, they will have little influence to the final evolution of the system, either in amplitude or relative phase.

VII. DISCUSSION AND CONCLUSION

In this paper, we have reported and interpreted a type of gravity water surface wave observed in a harmonically driven narrow water tank, which is alternately a localized Faraday wave. In the direction along the narrow sides, it is neither symmetric nor antisymmetric, but alternately having large oscillations on one side while almost flat on the opposite side, and vice versa. The spectrum of the DCT of the surface profile shows a clean two-mode domination [modes (12,0) and (8,1)], which contradicts the commonly observed localized waves that have fast decay but continuous spectrum [38].

We have adopted the nonlinear mode competition model to explain the phenomenon. In particular, in the linear approximation of the system without considering dissipation, one arrives at the Mathieu equation, where both modes (12,0) and (8,1) are unstable. If this is the case, their frequencies will be detuned to the same value due to the external driving, and only two values of the phase are possible for subharmonic response. Since dissipation is inevitable in the experiments [55,56], we have then considered dissipation effects in the system, which again yields a standard Mathieu equation. The effect of dissipation changes the parameter values for the modes, but the change is so small that it does not have discernible effects. The main contribution from dissipation is that the unstable region shrinks. As a result, the mode (8,1) is kicked out of the unstable region, and only mode (12,0) still remains unstable. But in the observed ALFW pattern, the amplitude of mode (8,1) is quite large. The reason lies in the nonlinear mode coupling from mode (12,0) to mode (8,1), which forms an internal resonant term for mode (8,1), making it unstable. This is indeed the case, as in the development of the ALFW pattern, mode (12,0) is always the first mode that gets excited, and only when its amplitude becomes large enough, mode (8,1) begins to emerge. The amplitudes of all the other modes remain close to zero. In addition, the relative phase of these two modes is locked by the nonlinear interactions, forming the stable ALFW pattern observed in the experiments.

From the nonlinear mode coupling equations for these two dominant modes and physical considerations, we have deduced the nonlinear mode competition equations, e.g., nonlinearly coupled Mathieu equations with self-nonlinear-interactions, which were first used by Gollub *et al.* [54]. The numerical simulations of this nonlinear coupled ODE model agree with the experimental data very well. This model explains the ALFW pattern completely, where the dissipation effect has been considered, the two modes are phase locked, and the amplitudes are bounded. Thus the internal nonlinear coupling between these two modes is revealed correctly. Furthermore, the boundary of the unstable region for the two modes can also be obtained by this model, which agrees with the experiments well.

Although mode (8,1) can be excited solely with a much larger driven amplitude, which is consistent with previous observations that the 1st modes in the narrow direction typically have larger dissipations than the 0th modes [4,5], in the parameter space shown in Fig. 8, mode (8,1) is stable by its own and its excitation is exclusively due to the nonlinear driving from mode (12,0). Therefore, the observed ALFW phenomenon is actually not exactly a two-mode competition, but a rather leading-passive pair of modes with mutual nonlinear interactions. Furthermore, even close to the region where (8,1) is the only mode that gets excited, the inverse pair where mode (8,1) is excited first and then it drives mode (12,0) unstable have not been observed in our experiment. A possible rationalization could be that in that case, since the dissipation for mode (8,1) is much larger than (12,0), mode (12,0) is always favorable and excites, if not earlier, no later than mode (8,1).

In short, the observed ALFW pattern has been explained well by the nonlinear mode competition model with two dominant modes, where only one mode can be excited directly by the external driving, and the excitation of the other mode is through strong nonlinear couplings with this excited mode. The good agreement between experiments and numerics validates the model and the physical picture.

As nonlinear mode coupling is quite common in realistic systems, we expect that our analytical approach could have broad applications in similar phenomena where nonlinear interactions between modes are non-negligible. Specifically, an ALFW-like pattern could exist in other gravity surface waves in high aspect ratio tanks. The combination of the 0th and the 1st modes in the narrow (y) direction is essential, and the natural frequencies of these two modes should be close. The ratio of the mode numbers m_1 and m_2 in the x direction should be $3:2$ for better visual effects. Higher modes in the y direction, with one even and one odd, and other ratios of the mode numbers in the x direction are also possible to yield similar phenomena, but lower modes are preferable as typically they have larger amplitudes and they are easier to be excited.

ACKNOWLEDGMENTS

We would like to thank Shengqiang Lai and Prof. Wenshan Duan for illuminating discussions. This work was supported by National Natural Science Foundation of China under Grants No. 11775101 and No. 11422541.

[1] M. Faraday, On a peculiar class of acoustical figures; and on certain forms assumed by groups of particles upon vibrating elastic surfaces, Philos. Trans. R. Soc. London **121**, 299 (1831).

[2] L. Rayleigh, XVII. On the maintenance of vibrations by forces of double frequency, and on the propagation of waves through a medium endowed with a periodic structure, Philos. Mag. **24**, 145 (1887).

[3] G. I. Taylor, An experimental study of standing waves, Proc. R. Soc. London A **218**, 44 (1953).

[4] S. Douady and S. Fauve, Pattern selection in Faraday instability, Europhys. Lett. **6**, 221 (1988).

[5] S. Douady, Experimental study of the Faraday instability, J. Fluid Mech. **221**, 383 (1990).

[6] H. Bredmose, M. Brocchini, D. H. Peregrine, and L. Thais, Experimental investigation and numerical modeling of steep forced water waves, J. Fluid Mech. **490**, 217 (2003).

[7] S. Residori, A. Guarino, and U. Bortolozzo, Two-mode competition in Faraday instability, Europhys. Lett. **77**, 44003 (2007).

[8] V. A. Kalinichenko and S. Ya. Sekerzh-Zen'kovich, Experimental investigation of Faraday waves of maximum height, Fluid Dyn. **42**, 959 (2007).
[9] X. Li, Z. Yu, and S. Liao, Observation of two-dimensional Faraday waves in extremely shallow depth, Phys. Rev. E **92**, 033014 (2015).
[10] É. Mathieu, Mémoire sur le mouvement vibratoire d'une membrane de forme elliptique, J. Math. Pure Appl. **13**, 137 (1868).
[11] N. N. Moiseev, On the theory of nonlinear vibrations of a liquid of finite volume, J. Appl. Math. Mech. **22**, 860 (1958).
[12] W.-H. Chu, Subharmonic oscillations in an arbitrary tank resulting from axial excitation, J. Appl. Mech. **35**, 148 (1968).
[13] J. W. Miles, Nonlinear surface waves in closed basins, J. Fluid Mech. **75**, 419 (1976).
[14] J. W. Miles, Nonlinear Faraday resonance, J. Fluid Mech. **146**, 285 (1984).
[15] V. G. Nevolin, Parametric excitation of surface waves, J. Eng. Phys. **47**, 1482 (1984).
[16] G. Sciortino, C. Adduce, and M. La Rocca, Sloshing of a layered fluid with a free surface as a Hamiltonian system, Phys. Fluids **21**, 052102 (2009).
[17] E. V. Buldakov, P. H. Taylor, and R. E. Taylor, New asymptotic description of nonlinear water waves in Lagrangian coordinates, J. Fluid Mech. **562**, 431 (2006).
[18] O. Agam and B. L. Altshuler, Scars in parametrically excited surface waves, Physica A **302**, 310 (2001).
[19] W. Zhang and J. Vinals, Pattern formation in weakly damped parametric surface waves, J. Fluid Mech. **336**, 301 (1997).
[20] J. B. Frandsen, Sloshing motions in excited tanks, J. Comput. Phys. **196**, 53 (2004).
[21] A. Cariou and G. Casella, Liquid sloshing in ship tanks: A comparative study of numerical simulation, Mar. Struct. **12**, 183 (1999).
[22] D. E. Horsley and L. K. Forbes, A spectral method for Faraday waves in rectangular tanks, J. Eng. Math. **79**, 13 (2013).
[23] D. Zhao, Z. Hu, G. Chen, S. Lim, and S. Wang, Nonlinear sloshing in rectangular tanks under forced excitation, Int. J. Naval Arch. Ocean Eng. **10**, 545 (2018).
[24] O. M. Faltinsen, O. F. Rognebakke, I. A. Lukovsky, and A. N. Timokha, Multidimensional modal analysis of nonlinear sloshing in a rectangular tank with finite water depth, J. Fluid Mech. **407**, 201 (2000).
[25] O. M. Faltinsen and A. N. Timokha, An adaptive multimodal approach to nonlinear sloshing in a rectangular tank, J. Fluid Mech. **432**, 167 (2001).
[26] P. Ferrant and D. Le Touze, Simulation of sloshing waves in a 3D tank based on a pseudo-spectral method, in *Proc. 16th Int. Workshop on Water Waves and Floating Bodies, Hiroshima, Japan* (http://www.iwwwfb.org/Workshops/16.htm, 2001), pp. 37–40.
[27] T. Ikeda, Autoparametric resonances in elastic structures carrying two rectangular tanks partially filled with liquid, J. Sound Vib. **302**, 657 (2007).
[28] I. Gavrilyuk, I. Lukovsky, Yu. Trotsenko, and A. Timokha, Sloshing in a vertical circular cylindrical tank with an annular baffle. Part 1. Linear fundamental solutions, J. Eng. Math. **54**, 71 (2006).
[29] M. C. Cross and P. C. Hohenberg, Pattern formation outside of equilibrium, Rev. Mod. Phys. **65**, 851 (1993).
[30] H. W. Müller, Periodic Triangular Patterns in the Faraday Experiment, Phys. Rev. Lett. **71**, 3287 (1993).
[31] B. Christiansen, M. T. Levinsen *et al.*, Ordered Capillary-Wave States: Quasicrystals, Hexagons, and Radial Waves, Phys. Rev. Lett. **68**, 2157 (1992).
[32] W. S. Edwards and S. Fauve, Patterns and quasi-patterns in the Faraday experiment, J. Fluid Mech. **278**, 123 (1994).
[33] A. Kudrolli, B. Pier, and J. P. Gollub, Superlattice patterns in surface waves, Physica D **123**, 99 (1998).
[34] J. Rajchenbach, D. Clamond, and A. Leroux, Observation of Star-Shaped Surface Gravity Waves, Phys. Rev. Lett. **110**, 094502 (2013).
[35] H. Arbell and J. Fineberg, Spatial and Temporal Dynamics of Two Interacting Modes in Parametrically Driven Surface Waves, Phys. Rev. Lett. **81**, 4384 (1998).

[36] H. W. Müller, R. Friedrich, and D. Papathanassiou, Theoretical and experimental investigations of the Faraday instability, in *Evolution of Spontaneous Structures in Dissipative Continuous Systems* (Springer, Berlin, Heidelberg, 1998), pp. 230–265.
[37] C. Wagner, H. W. Müller, and K. Knorr, Faraday Waves on a Viscoelastic Liquid, Phys. Rev. Lett. **83**, 308 (1999).
[38] J. Wu, R. Keolian, and I. Rudnick, Observation of a Nonpropagating Hydrodynamic Soliton, Phys. Rev. Lett. **52**, 1421 (1984).
[39] X. Li, D. Xu, and S. Liao, Observations of highly localized oscillons with multiple crests and troughs, Phys. Rev. E **90**, 031001 (2014).
[40] L. Kahouadji, N. Périnet, L. S. Tuckerman, S. Shin, J. Chergui, and D. Juric, Numerical simulation of supersquare patterns in Faraday waves, J. Fluid Mech. **772**, R2 (2015).
[41] I. Tadjbakhsh and J. B. Keller, Standing surface waves of finite amplitude, J. Fluid Mech. **8**, 442 (1960).
[42] S. Hayama, K. Aruga, and T. Watanabe, Nonlinear responses of sloshing in rectangular tanks: 1st report, nonlinear responses of surface elevation, Bull. JSME **26**, 1641 (1983).
[43] J. W. Miles, Surface-wave damping in closed basins, Proc. R. Soc. London A **297**, 459 (1967).
[44] J. Bechhoefer, V. Ego, S. Manneville, and B. Johnson, An experimental study of the onset of parametrically pumped surface waves in viscous fluids, J. Fluid Mech. **288**, 325 (1995).
[45] A. Kudrolli, M. C. Abraham, and J. P. Gollub, Scarred patterns in surface waves, Phys. Rev. E **63**, 026208 (2001).
[46] X. Hu, J. Yang, J. Zi, C. T. Chan, and K.-M. Ho, Experimental observation of negative effective gravity in water waves, Sci. Rep. **3**, 1916 (2013).
[47] J. Miles, Parametrically excited, standing cross-waves, J. Fluid Mech. **186**, 119 (1988).
[48] R. A. Ibrahim, *Liquid Sloshing Dynamics: Theory and Applications* (Cambridge University Press, Cambridge, 2005), pp. xix and 344.
[49] R. A. Ibrahim, Recent advances in physics of fluid parametric sloshing and related problems, J. Fluids Eng. **137**, 090801 (2015).
[50] G. Taylor, The instability of liquid surfaces when accelerated in a direction perpendicular to their planes. I, Proc. R. Soc. London A **201**, 192 (1950).
[51] D. J. Lewis, The instability of liquid surfaces when accelerated in a direction perpendicular to their planes. II, Proc. R. Soc London A **202**, 81 (1950).
[52] T. B. Benjamin and F. Ursell, The stability of the plane free surface of a liquid in vertical periodic motion, Proc. R. Soc. London A **225**, 505 (1954).
[53] N. W. Mclachlan, Application of Mathieu's equation to stability of non-linear oscillator, The Mathematical Gazette **35**, 105 (1951).
[54] S. T. Ciliberto and J. P. Gollub, Pattern Competition Leads to Chaos, Phys. Rev. Lett. **52**, 922 (1984).
[55] K. Kumar, Linear theory of Faraday instability in viscous liquids, Proc. R. Soc. London A **452**, 1113 (1996).
[56] P. Chen and J. Viñals, Amplitude equation and pattern selection in Faraday waves, Phys. Rev. E **60**, 559 (1999).
[57] J. Miles and D. Henderson, Parametrically forced surface waves, Annu. Rev. Fluid Mech. **22**, 143 (1990).
[58] S. T. Milner, Square patterns and secondary instabilities in driven capillary waves, J. Fluid Mech. **225**, 81 (1991).
[59] A. D. D. Craik and J. G. M. Armitage, Faraday excitation, hysteresis and wave instability in a narrow rectangular wave tank, Fluid Dyn. Res. **15**, 129 (1995).
[60] D. M. Henderson, Effects of surfactants on Faraday-wave dynamics, J. Fluid Mech. **365**, 89 (1998).
[61] S. Kumar and O. K. Matar, Parametrically driven surface waves in surfactant-covered liquids, Proc. R. Soc. London A **458**, 2815 (2002).
[62] See Supplemental Material at http://link.aps.org/supplemental/10.1103/PhysRevFluids.4.014807 for the relative error of the driven frequencies and amplitudes.
[63] D. M. Harris and J. W. M. Bush, Generating uniaxial vibration with an electrodynamic shaker and external air bearing, J. Sound Vib. **334**, 255 (2015).

[64] See Supplemental Material at http://link.aps.org/supplemental/10.1103/PhysRevFluids.4.014807 for the analysis of the effects of surface tension.

[65] T. Petrova and R. B. Dooley, Revised release on surface tension of ordinary water substance, in *Proceedings of the International Association for the Properties of Water and Steam, Moscow, Russia* (http://www.iapws.org/relguide/Surf-H2O.html, 2014).

[66] L. D. Landau and E. M. Lifshitz, *Course of Theoretical Physics, Vol. 1: Mechanics* (Pergamon Press, Oxford, 1978), p. 83.

[67] E. A. Cerda and E. L. Tirapegui, Faraday's instability in viscous fluid, J. Fluid Mech. **368**, 195 (1998).

[68] See Supplemental Material at http://link.aps.org/supplemental/10.1103/PhysRevFluids.4.014807 for details of fitting nonlinear and coupling coefficients.